# Role of operating and environmental conditions in determining molten pool dynamics during electron beam melting and selective laser melting

Yufan Zhao [a], Kenta Aoyagi [a,] *, Kenta Yamanaka [a], and Akihiko Chiba [a]

[a] *Institute for Materials Research, Tohoku University, 2-1-1 Katahira, Aoba-ku, Sendai 980-8577, Japan*

* Corresponding author. Ph.D.; Tel.: +81 022 2152452.

*E-mail address:* k.aoyagi@imr.tohoku.ac.jp (K. Aoyagi)

**Abstract**

Electron beam melting (EBM) and selective laser melting (SLM) are representative powder bed fusion additive manufacturing methods. Because EBM and SLM have different operating and environmental conditions, such as ambient pressure of the chamber, initial temperature, and heat source, they have molten pool dynamics. In this study, single-bead melting experiments using EBM and SLM were performed in conjunction with computational thermal-fluid dynamics simulations in high-energy conditions to highlight the differences in the molten pool dynamics of EBM and SLM. The experimental results reveal that SLM is more likely to melt in the keyhole mode than the EBM pool under nominally identical line energy. The simulations showed that the instantaneous maximum temperature of the SLM molten pool is much lower than that of the EBM molten pool. An increase in the preheating temperature is found to strengthen the vapor recoil pressure; however, the vapor recoil pressure under vacuum is maintained at a considerably low level in EBM. Compared to EBM, the high atmospheric pressure and multiple laser reflections during SLM significantly enhance the effect of the vapor recoil pressure on the melt surface. The findings of this study can be useful for the formulation of appropriate processing strategies for the two processes.

*Keywords:* Powder bed fusion; Vapor recoil pressure; Multiple laser reflections; Keyhole; Numerical simulation.

## 1. Introduction

The powder-bed fusion process is an essential type of metal additive manufacturing (AM) that can be used to fabricate high-precision metal parts with intricate and hollow structures. Electron beam melting (EBM) and selective laser melting (SLM) are representative powder-bed fusion processes that have been widely used in the aerospace, automotive, biomaterials, energy, and other industries [1][2]. EBM and SLM share similar working principles and their main differences are related to their operating and environmental conditions [3]. In EBM, high-speed incident electrons collide with materials, so that the kinetic energy of the electrons is converted to heat [4]. In SLM, the thermal energy, which is produced using focused laser photon beams, is partly absorbed by the materials and partly reflected [5]. Unlike lasers, electron beams penetrate deep into materials with almost no reflection [6]. Thus, EBM has higher energy efficiency. Concerning the environmental conditions, the EBM process is conducted under vacuum because gas molecules scatter the electrons. For example, a helium gas environment with a pressure of 0.2 Pa is used in the Arcam system, and a backfilled gas environment with a pressure of $10^{-4}$ Pa is used in the Freemelt system. The SLM process is performed under a nitrogen or argon gas flow with pressure near or above standard atmospheric pressure (101325 Pa). In addition, EBM is a hot process because preheating is applied to avoid powder smoke, whereas SLM is usually performed at room temperature.

Researchers have performed comparative studies of metal parts manufactured through EBM and SLM and confirmed that the differences between the two processes lead to significant variations in the forming quality [7], microstructure [8], mechanical properties [9], biocompatibility [10], and corrosion resistance [11] of the products. In particular, good forming quality must be ensured by reducing or suppressing voids and forming defects for the products to reach normal use standards. Improper processing strategies (such as excessively high or low energy input [12], inappropriate hatch distance and layer thickness [13], inhomogeneous powder layer [14], and unsuitable path planning [15][16]) can cause defects. More importantly, the stability of the molten pool plays a crucial role in defect suppression. Many types of defects are essentially related to the interaction of the energy beam with the material and the resulting molten pool dynamics [17][18][19]. The molten pool dynamics in both EBM and SLM involve multiple physical phenomena, including Marangoni/buoyancy convection, metal evaporation, capillary effect, and wetting action. The

Marangoni effect mainly drives the high-velocity fluid flow along the melt surface owing to the temperature-dependent surface tension, which also contributes to the depression of the melt surface [20][21]. Concerning the physical effects directly related to defect formation, past studies on energy-beam processing have demonstrated that the vapor recoil pressure can further depress the melt surface and even create keyhole-induced porosity due to intense vaporization under high-energy inputs [18][22]. Moreover, in laser processing, when a conically deep molten pool forms, multiple reflections occur in the melt surface within the depression [23]. As the reflection repeats, the absorbed laser power increases, causing the melt depression to become deeper and sharper. Such a deep and unstable molten pool may further lead to porosity [24].

Molten pool behaviors with heat transfer and fluid flow are highly transient and localized. Researchers usually apply multiphysics numerical models to simulate AM processing. Körner's group [25][26] studied the fundamental consolidation mechanisms in EBM by using the 2-D lattice Boltzmann method. Their results indicated that the hydrodynamics are related to defect formation. A team at Northwestern University [27][28] applied a 3D modeling method by using computational fluid dynamics to investigate defect formation during EBM and revealed the underlying physical mechanisms correlated to the forming quality. A team at Lawrence Livermore National Laboratory [29][30] proposed a highly resolved numerical model to account for the fluid flow effects related to the formation of pores, spattering, and denudation during SLM. These studies demonstrated that the multiphysics numerical simulation is a powerful tool for studying the molten pool dynamics.

The operating and environmental conditions of EBM and SLM, including ambient pressure, initial temperature (with or without preheating), and heat source characteristics, are quite different; this inevitably affects the interactions between the energy beam and the material as well as the resulting molten pool dynamics. The evolution of the molten pool based on the processing parameters of EBM and SLM has been extensively studied [31][32][33]. These studies were aimed at probing a suitable range of processing windows. Nevertheless, to highlight the differences in the interaction between energy beams and materials, attention should be paid to the molten pool behavior under high-energy conditions. However, these phenomena have seldom been studied. In particular, high-energy conditions tend to make the molten pool unstable, leading to the possibility of keyhole formation. A comparison of the tendencies and differences in defect formation during EBM and SLM under high-energy conditions was expected to reveal the influence of the environmental

conditions on the molten pool behavior. Therefore, in this study, single-bead melting experiments of a Co-28Cr-6Mo (CCM) alloy using EBM and SLM in conjunction with computational thermal-fluid dynamics (CtFD) simulations were performed under high-energy conditions to clarify the differences in the molten pool dynamics of EBM and SLM. By comparing the molten pool behaviors, the underlying physical mechanisms related to the molten pool instability were highlighted. CtFD simulations helped to identify the role of the operating and environmental conditions in determining the molten pool dynamics for the two processes. The results of this study are expected to be beneficial for the development of processing strategies with the goal of defect suppression.

## 2. Methodology

### *2.1 EBM and SLM processing*

To investigate the fundamental molten pool dynamics, single-bead melting experiments were conducted on CCM alloy baseplates without the interference of a stochastic powder layer. The composition of the CCM alloy is listed in Table 1. An Arcam® A2X (Arcam, GE Additive, Sweden) and a Concept Laser® M2 Cusing (Concept Laser, GE Additive, Germany) were used for the EBM and SLM experiments, respectively. Some technical data of the Arcam and Concept Laser systems are shown in Table 2. In the EBM process, a vacuum of 0.2 Pa was maintained in the process chamber, and the substrate was preheated to 1123 K, which is the standard preheating temperature for the CCM alloy. The SLM process was implemented under an argon atmosphere with an oxygen level below 0.4%. The initial temperature of the baseplate was room temperature (298 K). The focus offsets of the electron and laser beam were zero in both processes. In the EBM process, the focus offset, which is an additional current, is used to adjust the beam spot size by translating the focal plane from the zero position. Besides the focus offset, the electron beam size is also influenced by the beam current [34]. For simplicity, the effect of the beam current on the spot size was ignored in the simulation; thus, the minimum size in the technical data (Table. 2) was applied. Single-bead melting trials were conducted at power ($P$) = 800, 1000, and 1200 W and scan speed ($V$) = 100 mm/s for EBM, and $P$ = 240, 300, and 360 W and $V$ = 30 mm/s for SLM. The resulting line energies ($E_{\text{line}} = P/V$) were 8, 10, and 12 J/mm, which were relatively high-energy inputs for both processes.

**Table 1**. Chemical composition of the Co-28Cr-6Mo alloy substrate.

| Composition | Cr | Mo | Ni | Fe | Si | Mn | C | N | Co |
|---|---|---|---|---|---|---|---|---|---|
| Value (wt.%) | 27.7 | 6.1 | 0.02 | 0.05 | 0.57 | 0.6 | 0.05 | 0.1 | Bal. |

**Table 2**. Technical data of the Arcam and Concept Laser systems.

| Machine | Arcam A2X [35] | Concept Laser M2 Cusing [36] |
|---|---|---|
| Beam power (W) | 50 ~ 3000 | 200 (fibre laser), 400 (optional) |
| Beam spot size (FWHM, μm) | 200 ~ | 50 ~ 200 |
| Beam scan speed (m/s) | ~ 8000 | ~ 7 |
| Production speed ($cm^3/h$) | ~ 80 | 2 ~ 20 |
| Chamber environment | He (~ 0.2 Pa) | Argon/$N_2$ atmosphere (101325 Pa) |
| Operating condition | preheating | room temperature |
| Surface finish (vertical/horizontal) | Ra15/Ra6 [37] | Ra4/Ra10 |

*2.2 Material characterization*

The single-bead profile was measured using a Keyence® VR-3200 3D measurement system (Keyence Co., Osaka, Japan). The samples were cut perpendicularly using a wire electric discharge machine. After grinding and polishing by standard metallographic techniques, the sectioned samples were etched for 30 s using a solution of HCl/$H_2O_2$ (6:1). Optical microscopy (OM) was utilized to observe the molten pool shape. The internal defects within the melt region were detected and visualized using an X-ray computed tomography (X-CT) system (Comscantecno Co., Ltd, Yokohama, Japan). The 3D rendering of X-CT data was conducted using ExFact® VR software (Nihon Visual Science, Inc., Tokyo). The measurement conditions and related parameters of the X-CT measurement are described in the Appendix.

*2.3 Numerical simulations*

3D transient CtFD models with multiphysics were developed using the commercial *Flow 3D*® [38] coupled with the plug-in *Flow weld* module, which is widely used in studies on AM heat transfer and fluid flow [39][40]. Exclusive physical models of the EBM and SLM processes were introduced to accurately track the molten pool dynamics and fluid-free surface. To solve the precise

fluid flow, buoyancy and Marangoni convection were realized by introducing a temperature-dependent density and surface tension, respectively. Moreover, the vapor recoil pressure $p_{\mathrm{recoil}}(T)$, which has an essential influence on the fluid stability (Fig. 1a), was evaluated, and its pressing effect on the melt surface was executed in the simulation [41]:

$$p_{\mathrm{recoil}}(T) = Ap_0 \exp\left[\frac{\Delta H_{\mathrm{LV}}(T - T_{\mathrm{V}})}{RTT_{\mathrm{V}}}\right], \tag{1}$$

where $p_0$ denotes the ambient pressure (Pa), which varies under the environment of EBM and SLM, $\Delta H_{\mathrm{LV}}$ is the vaporization latent heat (J/kg), $T_{\mathrm{V}}$ is the saturated vapor temperature (K), and $R$ is the universal gas constant (J/K·mol). The coefficient $A$ is generally assumed to be 0.54 [42], which suggests that 54% of the vapor pressure is equal to the recoil pressure. The relation between the saturated vapor pressure $p_{\mathrm{sat}}$ (Pa) and the corresponding saturated vapor temperature $T_{\mathrm{V}}$ (K) is governed by the Clausius–Clapeyron equation:

$$p_{\mathrm{sat}}(T_{\mathrm{V}}) = p_{V1} \exp\left[\frac{k\Delta H_{\mathrm{LV}}}{(k-1)C_{\mathrm{P}}}\left(\frac{1}{T_{\mathrm{V1}}} - \frac{1}{T_{\mathrm{V}}}\right)\right], \tag{2}$$

where $p_{V1}$ (Pa) and $T_{\mathrm{V1}}$ (K) denote the pressure-boiling point pair at any given pressure. In the simulation, the values of $p_{V1}$ and $T_{\mathrm{V1}}$ were applied as the standard atmospheric pressure and the corresponding boiling point; $k$ is the ratio of the heat capacity (J/kg·K) at a given pressure $C_{\mathrm{P}}$ to the heat capacity at a given volume $C_{\mathrm{V}}$; in particular, $T_{\mathrm{V}}$ (boiling point) is a function of $p_{\mathrm{sat}}$ (ambient pressure).

To trace the heat transfer in the simulation, besides thermal conduction, heat radiation and heat loss through evaporative cooling were activated (see the Appendix). In SLM, the heat source of a laser beam was approximated with a Gaussian energy distribution and only the irradiated material surface was considered [39]:

$$q(r) = \frac{2P}{\pi r_0^2} \exp\left(-\frac{2r^2}{r_0^2}\right), \tag{3}$$

where $q$ is the heat flux (W/m$^2$), $r$ is the radial distance from the beam center (m), $r_0$ is the actual beam radius (m), and $P$ is the beam power (W). Notably, as a volumetric heat source, the penetration depth $z$ (m) in the vertical direction of the electron beam energy in the EBM was considered. The energy distribution in the depth direction is modeled as [43]

$$e(z) = e_0\left(1 - \frac{z}{h_0}\right), \tag{4}$$

where $e$ is the internally absorbed power per unit volume (W/m$^3$), and $h_0$ and $e_0$ are the maximum penetration depth of the electron beam (m) and the corresponding power density, respectively. To satisfy $q = \int_0^{h_0} e\,dz$, $e_0$ must equal $(2/h_0) \cdot q$. Thus,

$$e(z) = \frac{2}{h_0}\left(1 - \frac{z}{h_0}\right)\frac{2P}{\pi r_0^2}\exp\left(-\frac{2r^2}{r_0^2}\right). \tag{5}$$

In addition, the multiple reflection effect of the laser results in an increased energy absorption rate (Fig. 1b) and plays an essential role during molten pool formation in SLM. The multiple laser reflections were implemented in the SLM simulation and coupled with the Fresnel energy absorption model [44], which governs the portion of energy absorbed from the reflected laser ray. The unabsorbed power due to reflected heat flux $Q_r$ (W/m$^2$) depends on the deviation angle $\varphi$ between the incident ray and surface normal:

$$Q_r = \frac{1}{2}\left(\frac{1 + (1 - \varepsilon\cos\varphi)^2}{1 + (1 + \varepsilon\cos\varphi)^2} + \frac{\varepsilon^2 - 2\varepsilon\cos\varphi + 2(\cos\varphi)^2}{\varepsilon^2 + 2\varepsilon\cos\varphi + 2(\cos\varphi)^2}\right), \tag{6}$$

where $\varepsilon$ is a coefficient related to the material properties and laser type. In the simulation, when the reflected energy is less than 0.01 times the initially incident energy, the reflection is terminated. Unlike SLM, electrons are almost entirely absorbed and penetrate into the material in contact during EBM [7][45]. Hence, reflection was not considered in the EBM modeling. For simplicity, the gas flow field with associated transport phenomena by gas or plasma during SLM was not modeled. The atmospheric flow contributes to particle or spatter motion in the SLM building chamber [46], which influences the surface roughness and molten pool stability owing to the variation in laser power delivered to the material surface [47][48]. Because the study of transport phenomena can be regarded as separate systematic research, the present study mainly focused on the direct effects of the surface on the resultant molten pool dynamics during EBM and SLM.

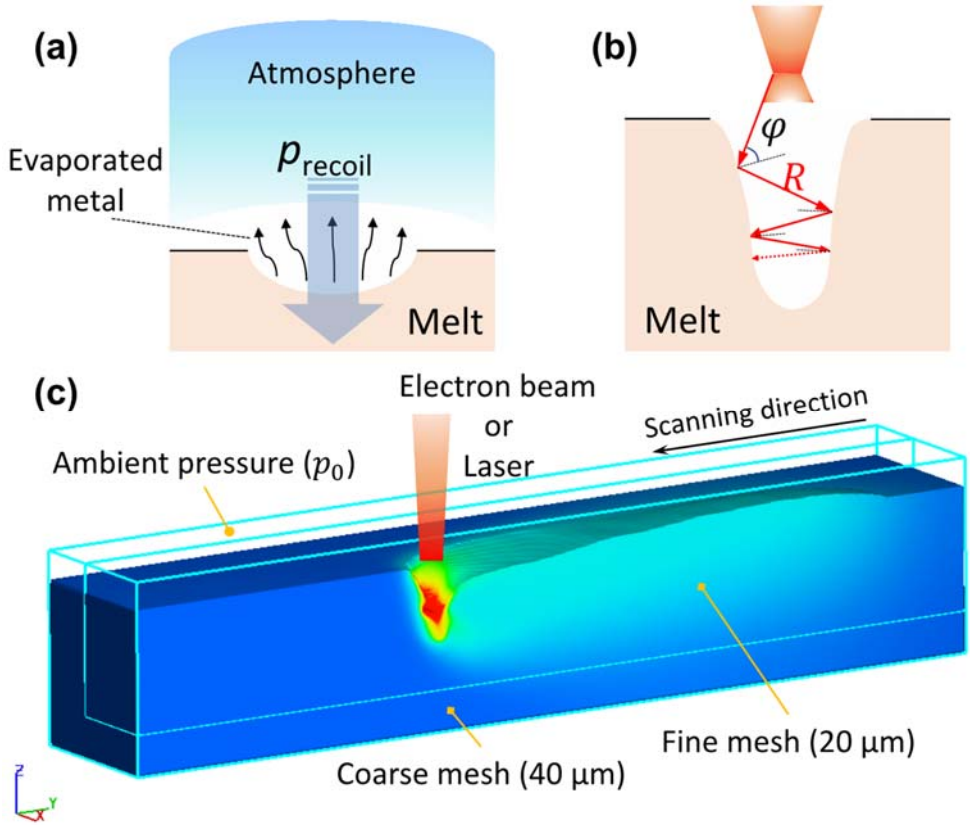


**Fig. 1.** Schematics of physical effects in the CtFD model containing (a) vapor recoil pressure in both EBM and SLM, and (b) multiple laser reflections in the keyhole during SLM. (c) Computational domain with biased mesh.

As shown in Fig. 1c, to compromise the calculation accuracy and efficiency, we applied a biased mesh containing a finer mesh of 20 μm (roughly equal the actual spatial resolution of X-CT) around the melted region and a coarser mesh of 40 μm in the rest of the baseplate. A void region without a fluid mass was located above the material and possessed a uniform pressure. The domain top was assigned as a pressure boundary, which represented the ambient pressure. Additional descriptions of the modeling physics, material thermophysical properties, and modeling validation of the CtFD simulation can be found in the Appendix.

## 3. Results

### *3.1 Single-bead characterization*

The single-bead profiles processed with EBM and SLM were visualized under three sets of processing conditions. The top and side views of the stereoscopic images are shown in Fig. 2. Under

nominally identical $E_{\text{line}}$, the melt beads processed by EBM were wider than those processed by SLM because the beam spot size of the focused laser was usually finer than that of the electron beam (Table 2). It is noteworthy that as $E_{\text{line}}$ increased to 12 J/mm, humping appeared along the melt bead processed by SLM. The surface humping formed under high-energy conditions was different from balling or melt fragmentation, resulting from insufficient penetration and action of the surface tension under low-energy (high scanning speed) conditions [49], which indicates the fluid flow within the molten pool was highly unstable.

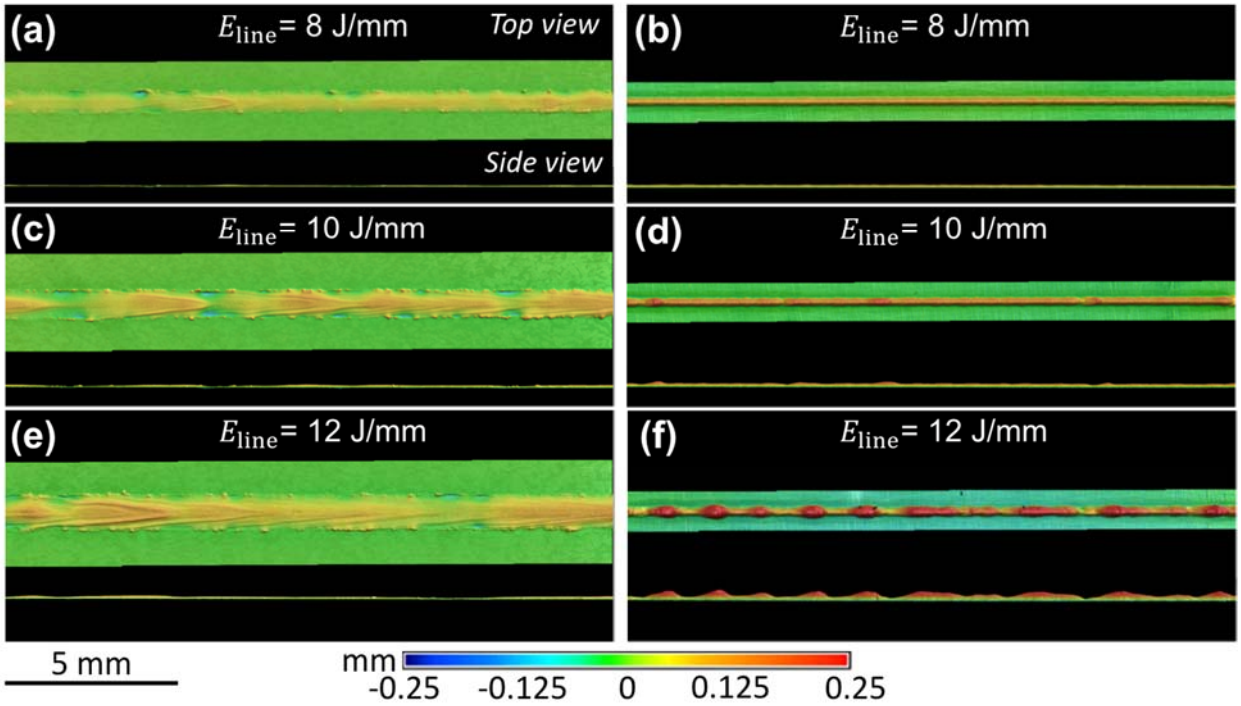


**Fig. 2.** Top and side views of the stereoscopic images showing the single-bead profiles processed by (a)(c)(e) EBM and (b)(d)(f) SLM under $E_{\text{line}}$ of (a)(b) 8, (c)(d) 10, and (e)(f) 12 J/mm.

As shown in Fig. 3, the single-bead samples were sectioned and examined by OM. The corresponding width, depth, and width/depth ratio of the melt region were measured from the OM images (Fig. 3a, b, d, e, g, h). The energy absorption efficiency of the electron beam (up to 90% [50]) is higher than that of the laser beam (up to 60% [51]); moreover, preheating was adopted in EBM. The application of preheating in EBM increases the thermal conductivity of the material [52], which has a positive effect on the expansion of the molten pool. Therefore, the area of the melt region (or the molten pool volume) processed by EBM was much larger than that processed by SLM under nominally identical $E_{\text{line}}$; this also indicated by the high deposition rate for EBM. With an increase

in $E_{\text{line}}$, the width and depth of the melt regions processed by both EBM and SLM increased. Notably, compared with EBM, SLM produced melt regions with considerably small width/depth ratios, which indicates that SLM tended to generate a narrow and deep molten pool with keyhole shapes under high-energy conditions [53]. The difference in the melt region shapes of EBM and SLM suggests that even if the energy absorption rate by the material of the electron beam was higher than that of the laser, EBM tended to maintain melting in the conduction mode, whereas SLM was more likely to induce melting in the keyhole mode under high-energy conditions.

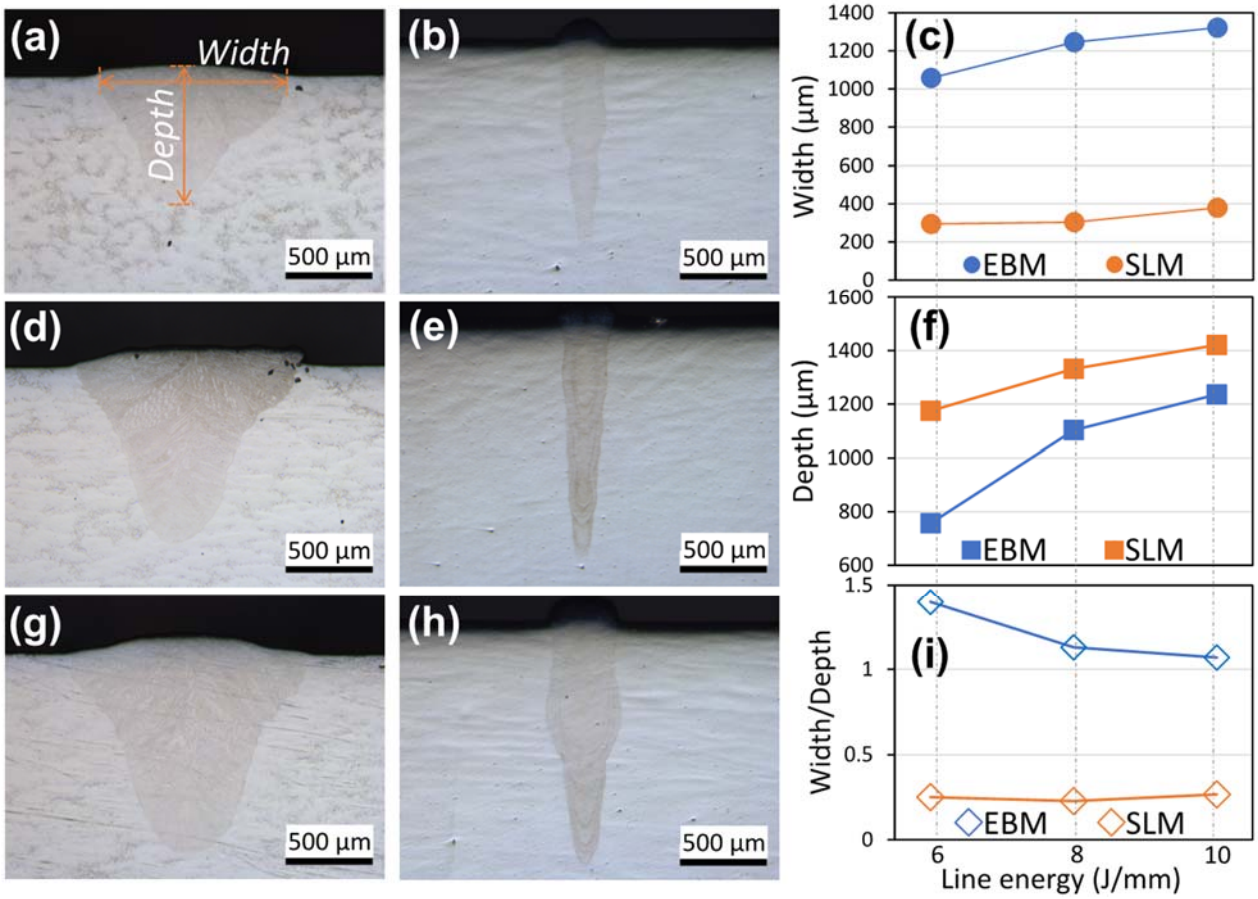


**Fig. 3.** OM images showing the sectioned single-bead samples processed by (a)(d)(g) EBM and (b)(e)(h) SLM under $E_{\text{line}}$ of (a)(b) 8, (d)(e) 10, and (f)(h) 12 J/mm. The corresponding (c) width, (f) depth, and (i) width/depth ratio of the melt region were measured from these OM images.

The internal defects within the melt region were examined using the X-CT technique. Fig. 4 shows 3D images of the X-CT measurements of the single-bead samples in which pores larger than 21 µm (this is the actual spatial resolution, which is approximately three times the nominal resolution) can be detected. Under the three energy input conditions, almost no pores were detected in the EBM samples. By contrast, in the SLM samples under $E_{\text{line}}$ of 8 and 10 J/mm, some small

pores appeared sporadically. In particular, for $E_{\text{line}}$ of 12 J/mm, conspicuously large pores with irregular spherical shapes were continuously arranged in the melt region along the scanning direction. Therefore, in this study, we focused on examining the reasons why such pores were absent in the samples processed by EBM, considering that the electron beam possessed a higher energy absorption rate than the laser beam and excessively high energy input usually leads to molten pool instability and defect formation. The samples were processed under the same $E_{\text{line}}$ so that differences in the bead profile, molten pool shape, and internal defect were assumed to be due to the distinct molten pool dynamics.

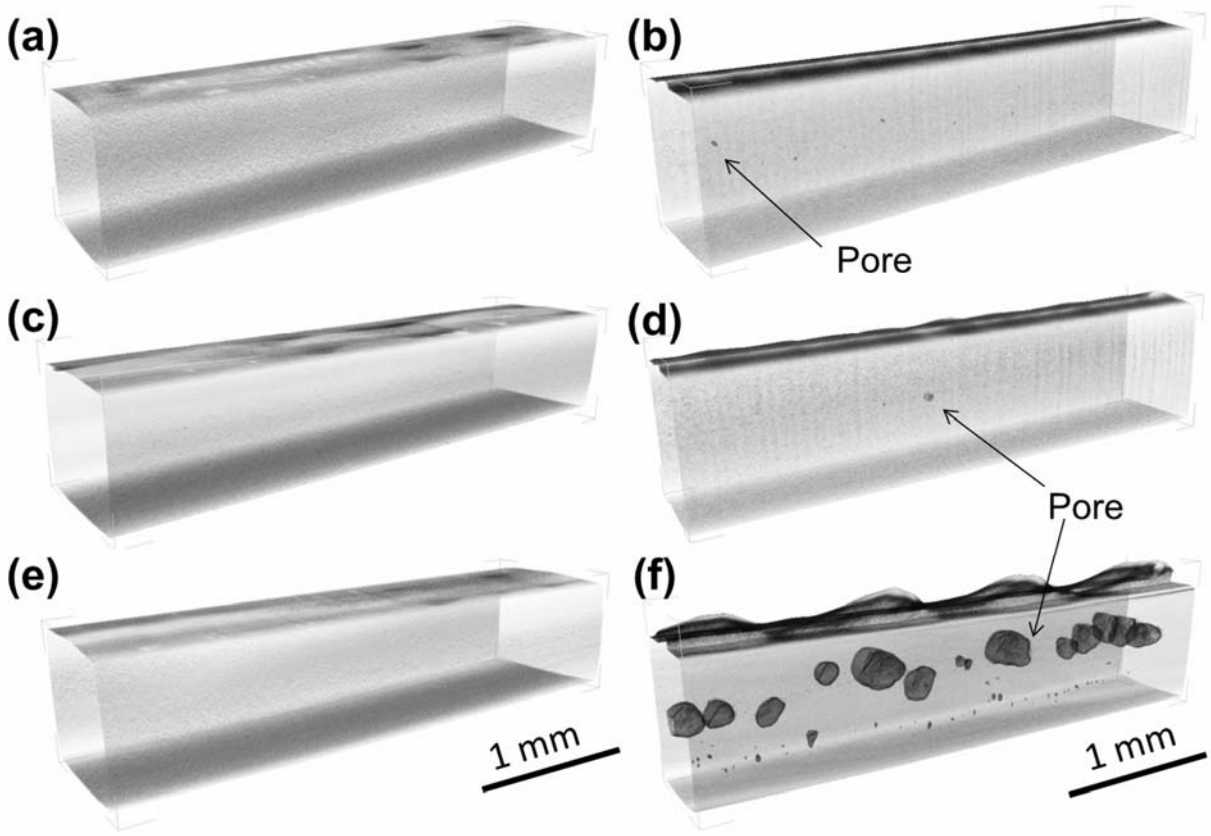


**Fig. 4.** 3D images of X-CT measurements of single-bead samples processed by (a)(c)(e) EBM and (b)(d)(f) SLM under $E_{\text{line}}$ of (a)(b) 8, (c)(d) 10, and (e)(f) 12 J/mm.

### *3.2 Single-bead simulation*

Numerical simulations helped to provide insight into the molten pool dynamics and physical effects influencing the bead profile, molten pool shape, and internal defects. The longitudinal cross-sections of the CtFD simulated melt beads with temperature contours during melting are shown in

Fig. 5. Multiphysics, including buoyancy/Marangoni convection and vapor recoil pressure for both EBM and SLM, and multiple laser reflections for SLM, were activated in the simulations. According to whether preheating was performed, the initial temperature of the computational domains was 1123 K for EBM and 298 K for SLM. Under two sets of processing conditions, the depressed molten pool front was presented for both the EBM and SLM. The ratio of opening size to depth of the melt depression processed by EBM was greater than that of the melt depression processed by SLM, indicating a weak trend of defect formation during EBM. When $E_{\mathrm{line}}$ was increased to 12 J/mm, the depression of the molten pool further deepened for both the EBM and SLM. Notably, continuously arranged pores appeared in the melt bead processed by SLM, showing close agreement between the simulation (Fig. 5d) and experiment (Fig. 4f). According to the simulated temperature fields, EBM showed a molten pool with a higher temperature than SLM. The instantaneous maximum temperatures ($T_{\mathrm{max}}$) in the EBM molten pool were 6503 K ($E_{\mathrm{line}}$= 8 J/mm) and 8596 K ($E_{\mathrm{line}}$= 12 J/mm), which were higher than those in the SLM molten pool, i.e., 2988 K ($E_{\mathrm{line}}$= 8 J/mm) and 3055 K ($E_{\mathrm{line}}$= 12 J/mm). Evaporation is a kinetic process. Similarly, in the simulation, if the melt temperature $T$ at the free surface at time step 1 exceeds the boiling point $T_{\mathrm{V}}$, the liquid evaporates at a rate $\Gamma$ (kg/s) at the following time steps:

$$\Gamma = \alpha A_{\mathrm{sur}} \left[ \frac{\kappa (T - T_{\mathrm{V}})}{h \Delta H_{\mathrm{LV}}} \right], \tag{7}$$

where $\alpha$ is an accommodation coefficient, $A_{\mathrm{sur}}$ is the effective surface area for phase change ($m^2$), and $h$ is a characteristic length for heat conduction in the liquid at the surface (m). Since in the model, evaporation only occurs at the computational grid located on the free surface. The non-surface high-temperature (over boiling point) melt will evaporate after the evaporation of the surface melt. As a result, the non-surface high-temperature melt can continue to exist for a certain period. Thus, it is reasonable for the instantaneous temperature of the melt to exceed the boiling point in the simulation. On the one hand, the electron beam, with high energy efficiency and a preheating process, allows the EBM molten pool to rise quickly to extremely high temperatures. This superheating effect contributes to the microstructure refinement in EBM-built aluminum-silicon eutectic alloys [54]. On the other hand, compared with EBM, the intensified heat convection caused by the unstable molten pool made it difficult to maintain the high temperature of the SLM molten pool.

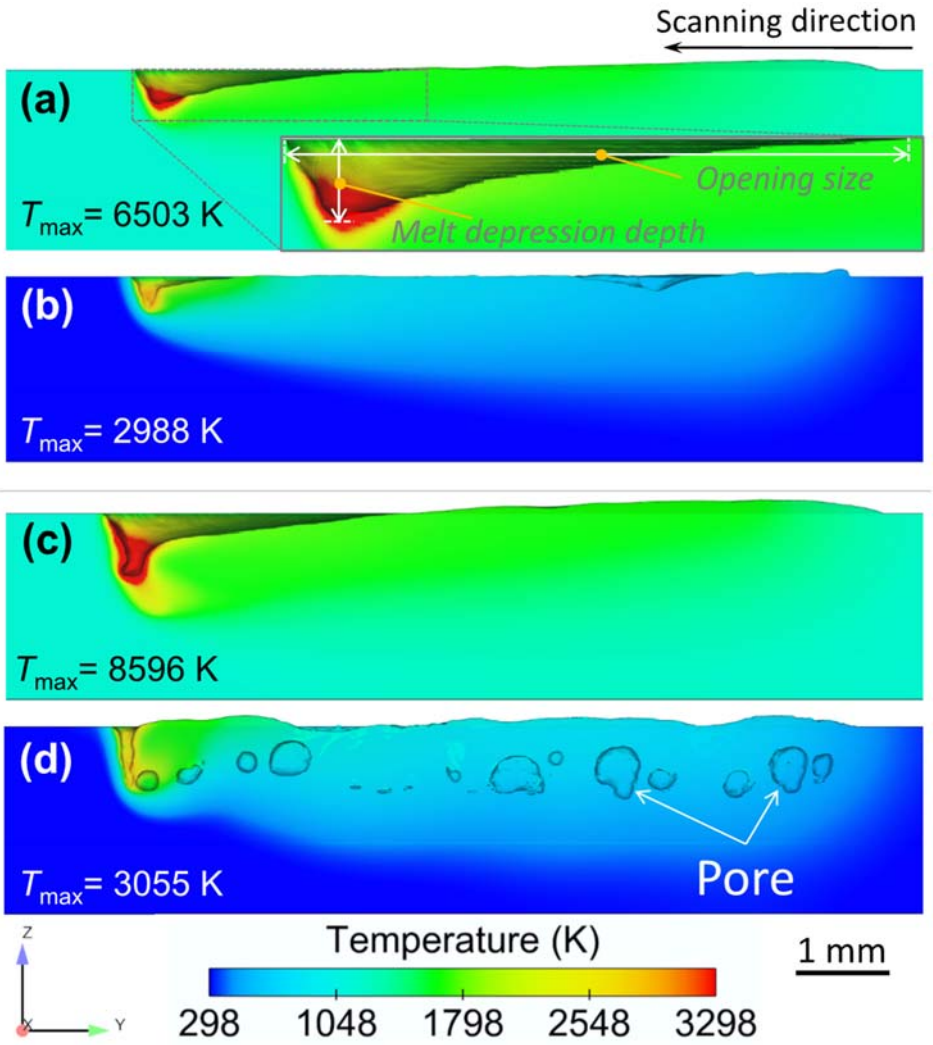


**Fig. 5.** Longitudinal cross-sections of the CtFD simulated melt beads with temperature contour during (a)(c) EBM and (b)(d) SLM under $E_{\text{line}}$ of (a)(b) 8 and (c)(d) 12 J/mm.

The precise mechanism of pore formation during SLM was investigated through simulations. The complete process of pore formation is shown in Fig. 6. When the depression of the molten pool was created and deepened continuously, the bottom melt flowed counterclockwise to the upper part. As the molten pool advanced, the continuous accumulation of the melt eventually collapsed from the depression surface and wrapped the bottom cavity to form pores. Such irregular sphere-like pores were identified as typical keyhole-induced pores. These pores form during keyhole-mode melting when the metal evaporation-induced cavity is trapped by keyhole collapse [55]. These pores are initially filled with the metal vapor and become vacuum voids after cooling and solidification. Thus, with the increase in $E_{\text{line}}$, the amount of metal evaporation and the depth of the melt depression

increase. This reduces the stability of the keyhole, thereby forming keyhole pores in the melt bead processed by SLM.

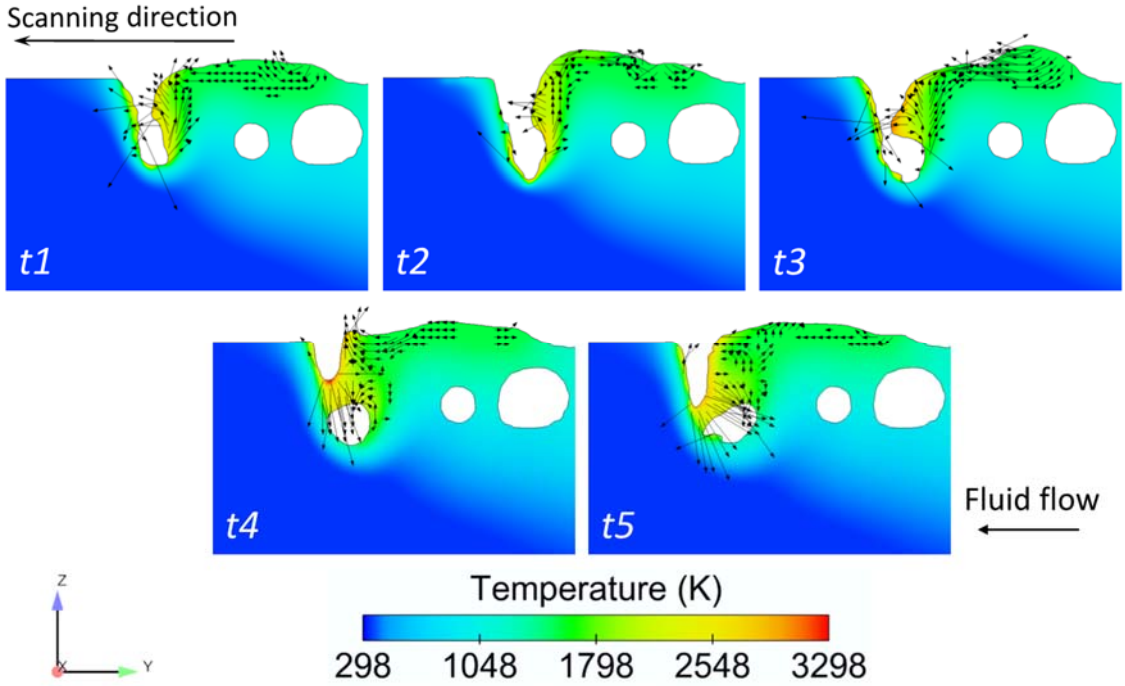


**Fig. 6.** CtFD simulated process of keyhole-induced pore formation during SLM melting with $E_{\mathrm{line}}$ of 12 J/mm over time.

## 4. Discussion

The ambient pressure in the building chamber, initial temperature (with or without preheating), and absorption and interaction of materials with energy beams during EBM and SLM are different. Therefore, in the following discussion, the influences of the operating and environmental conditions on the physical actions related to molten pool instability and defect formation are examined in terms of the artificial operability through simulations. The comparative simulations were arranged as follow:

- *4.1 Influence of ambient pressure*: Based on the original EBM simulation result, a comparison was conducted by changing the ambient pressure (vacuum and standard atmospheric pressure).
- *4.2 Influence of initial temperature*: Based on the simulation results discussed in Section 4.1, a comparison was conducted by changing the initial temperatures under vacuum and standard atmospheric pressure.

- *4.3 Influence of absorption and interaction of energy beam with materials*: Based on the original SLM simulation results, a comparison was conducted with and without multiple laser reflections.

Because the essential difference in the modeling between typical EBM and SLM is the ambient pressure and initial temperature, it was feasible to conduct comparative simulations between EBM and SLM. Regardless of the process (EBM or SLM) used in the simulation, the same qualitative simulation results were obtained.

### *4.1 Influence of ambient pressure*

During the interaction of the energy beam with the material, keyhole formation is generally associated with the metal evaporation-induced recoil pressure. According to a previous study [56], the molten pool behavior processed by EBM is dominated by the Marangoni effect. Rather than the vapor recoil pressure, the depressed molten pool front is driven by a steady backward Marangoni flow along the melt surface because, in addition to the momentum conservation between the metal vapor and the melt, the counterforce exerted by the atmosphere on the metal vapor is a significant source of the vapor recoil pressure. As shown in Eq. (1), the magnitude of the vapor recoil pressure is related to the ambient pressure $p_0$. The high-vacuum environment in EBM may significantly weaken the effect of the vapor recoil pressure. Therefore, it is worth studying the impact of $p_0$ on the keyholes and accompanying defect formation.

By performing simulations, the influence of $p_0$ in EBM was examined with the same *P* and *V*. To control the variables, the scattering effect of the chamber pressure on the spot size change of the electron beam was neglected, i.e., the beam spot size remained unchanged. Fig. 7 shows the CtFD-simulated EBM melt beads processed with $E_{\mathrm{line}}$ of 12 J/mm under vacuum (0.2 Pa) and standard atmospheric pressure (101325 Pa). According to the simulated temperature fields, the instantaneous maximum temperatures ($T_{\max}$) of the molten pool under vacuum were higher than those under standard atmospheric pressure. The dimensionless Peclet number (*Pe*) can be used to evaluate the dominant heat transfer process (heat convection or heat conduction). *Pe* is the ratio of the heat convection rate to the heat conduction rate, and is expressed as [57]

$$Pe = \frac{heat\ convection}{heat\ conduction} = \frac{v\rho C_{\mathrm{p}}\Delta T}{\kappa \Delta T / L_{\mathrm{R}}} = \frac{v\rho C_{\mathrm{p}} L_{\mathrm{R}}}{\kappa}, \tag{8}$$

where $v$ is the fluid velocity (m/s), $\rho$ is the density (kg/m$^3$), $C_\mathrm{p}$ is the specific heat (J/kg·K), $\kappa$ is the thermal conductivity ($\mathrm{W/m \cdot K}$), $\Delta T$ is the difference between the maximum temperature and liquidus (K), and $L_\mathrm{R}$ is the characteristic length (m). The average magnitudes of $v$ and $L_\mathrm{R}$ (mean of the molten pool width and depth) during melting were applied. Fig. 8 shows the *Pe* value as melting proceeded under vacuum and standard atmospheric. Under 101325 Pa, the *Pe* values oscillated and were higher than those under vacuum, which indicates that the heat transfer was dominated by convection in the case of standard atmospheric pressure. Thus, the heat accumulated in the molten pool was effectively dissipated owing to the instability of the molten pool, and the heat convection intensified under standard atmospheric pressure. Accordingly, in addition to the low energy efficiency of the laser beam, intense heat convection driven by the SLM processing environment makes the instantaneous maximum temperatures of the SLM molten pool much lower than those of the EBM molten pool (Fig. 5).

Under standard atmospheric pressure (Fig. 7b), the depressed molten pool front was much deeper than that under vacuum. In addition, surface irregularities and internal pores appeared under standard atmospheric pressure. According to Eq. (2), the boiling point of the metal is lower under the low-pressure condition. The reduction in the boiling point contributes to the increase in the evaporation, as verified by Bidare et al. [58]. Then, the maximum vapor recoil pressure (Max. VPR) at each time step was collected from one batch of the simulation. However, from the statistical values of the maximum vapor recoil pressure in the two cases during melting (Fig. 9), the magnitude under standard atmospheric pressure was found to be two to three orders of magnitude higher than that under vacuum. High ambient pressure significantly aggravated the effect of the vapor recoil pressure on the melt surface. Deep melt depression, formed under high recoil pressure, increased the instability of the melt surface, creating surface irregularities and keyhole-induced porosity.

Because the ambient pressure is critical in determining the vapor recoil pressure, SLM under vacuum can effectively suppress defects. As illustrated in a recent study [59] on the chamber pressure in SLM, compared with the processing under argon atmosphere, the vacuum environment significantly inhibited keyhole formation when excessive energy input was not applicable, which is consistent with the present simulation. For improving the forming quality of the SLM-built sample by reducing the chamber pressure, it is better to avoid inputting excessively high energy. An

excessive energy input will induce excessive evaporation, counteracting the weakening effect of the low chamber pressure on the vapor recoil pressure. In particular, owing to the reduction in the boiling point of the metal under low chamber pressure, additional devices are needed to protect the laser lens from contamination from the metal vapor, e.g., a protective working lens placed in front of the sealed lens and cleaned by a brush [60].

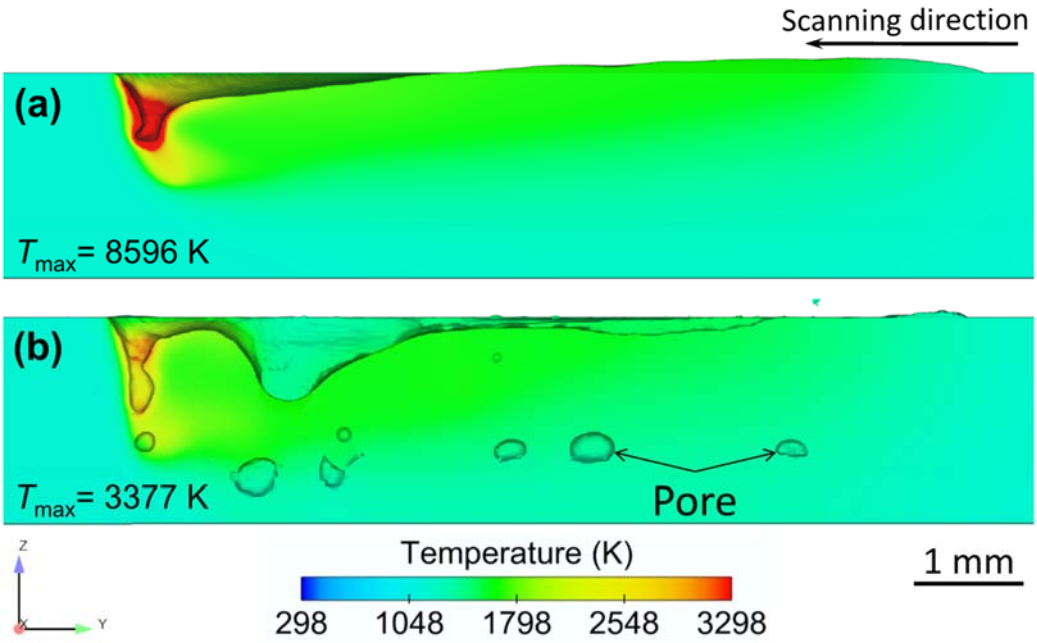


**Fig. 7.** CtFD simulated EBM melt beads processed with an $E_{\mathrm{line}}$ of 12 J/mm and an initial temperature of 1123 K under (a) vacuum (0.2 Pa) and (b) standard atmospheric pressure (101325 Pa).

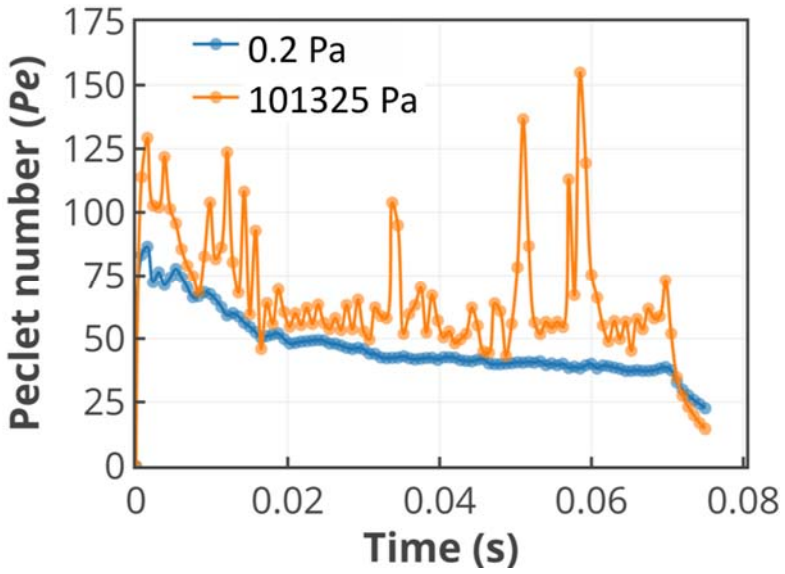


**Fig. 8.** Peclet number as a function of time during the simulations of melt beads processed with an $E_{\mathrm{line}}$ of 12 J/mm under vacuum (0.2 Pa) and standard atmospheric pressure (101325 Pa).

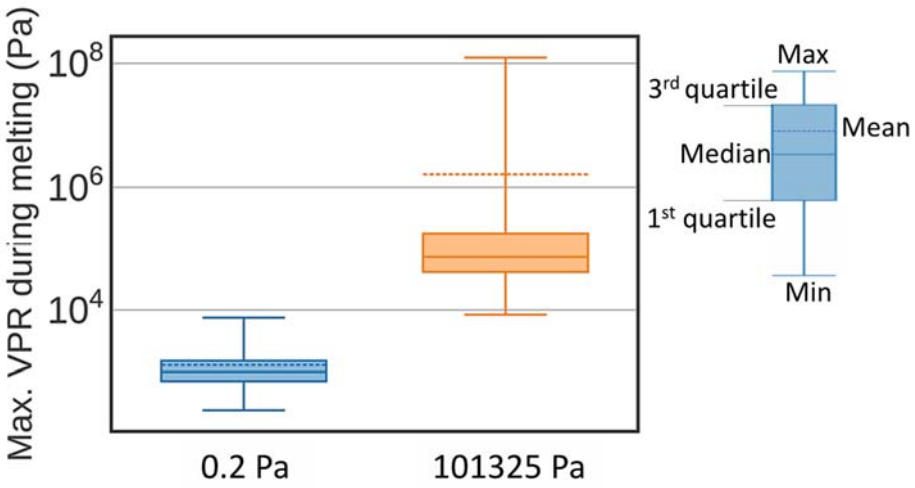


**Fig. 9.** Statistical values of the maximum vapor recoil pressure during EBM melting under vacuum (0.2 Pa) and standard atmospheric pressure (101325 Pa) and an $E_{\mathrm{line}}$ of 12 J/mm.

*4.2 Influence of initial temperature*

To investigate the influence of the initial temperature on the molten pool behavior, a set of simulations without preheating (room temperature, 298 K) were implemented and compared with the corresponding simulations performed with preheating (1123 K), as discussed in Section 4.1. Fig. 10 illustrates the CtFD-simulated EBM melt beads without preheating under vacuum and standard atmospheric pressure. As in the case shown in Fig. 7, a defect appeared in the case of standard atmospheric pressure. Importantly, a comparison of Fig. 7b and Fig. 10b reveals that under standard atmospheric pressure, the tendency of defect formation increased as the initial temperature increased. However, a comparison of Fig. 7a and Fig. 10a shows that under vacuum, there was no noticeable variation in the molten pool behavior, which indicates that the ambient pressure affects the melt depression during melting more than the initial temperature. Moreover, a comparison of Fig. 7 and Fig. 10 reveals that the effect of the high initial temperature (application of preheating) on the increase in the instantaneous maximum temperatures of the molten pool is relatively small, indicating that the heat convection driven by the fluid flow significantly affects the molten pool temperature. By comparing the simulation results of the maximum vapor recoil pressure at the two initial temperatures (Fig. 11a), it can be seen that increase in the initial temperature strengthened the vapor recoil pressure to a certain extent. As shown in Fig. 11b and c, such enhancements in the vapor recoil pressure were due to the increase in the metal evaporation rate with the increase in the initial

temperature. Preheating has been shown to increase the thermal conductivity, which improves the efficiency of the heat transfer during beam–matter interactions [52][61]. Thus, a high initial temperature causes the molten metal to quickly heat above the boiling point. However, the vapor recoil pressure under vacuum was considerably low both when preheated and when not preheated. In addition, the severe oscillation of the evaporation rate under atmospheric pressure shown in Fig. 11c also illustrates the molten pool instability determined by the vapor recoil pressure. The unstable melt surface was accompanied by a drastic change in the surface area irradiated by the electron beam, which caused oscillations in the evaporation rate. Thus, owing to the decisive role of the ambient pressure, the vapor recoil pressure was particularly sensitive to the initial temperature under standard atmospheric pressure. Generally, for SLM under standard atmospheric pressure, preheating to increase the initial temperature is beneficial for reducing stress and suppressing cracks [62]. However, the simulation results show that the application of preheating also increases the evaporation rate, as well as the vapor recoil pressure and hence, the probability of keyhole-induced porosity formation. A recent study [63] showed that the amount of evaporated metal was increased by preheating the baseplate in SLM. Another survey on single-track melting by SLM [64] revealed that the preheating contributed to the instability of the melt track. The results of these studies are consistent with the present simulation results. Moreover, preheating has been shown to accelerate the powder degradation with increased oxygen content [65]. Therefore, to prevent defects, the preheating temperature for SLM must be chosen carefully, and preheating under vacuum is recommended.

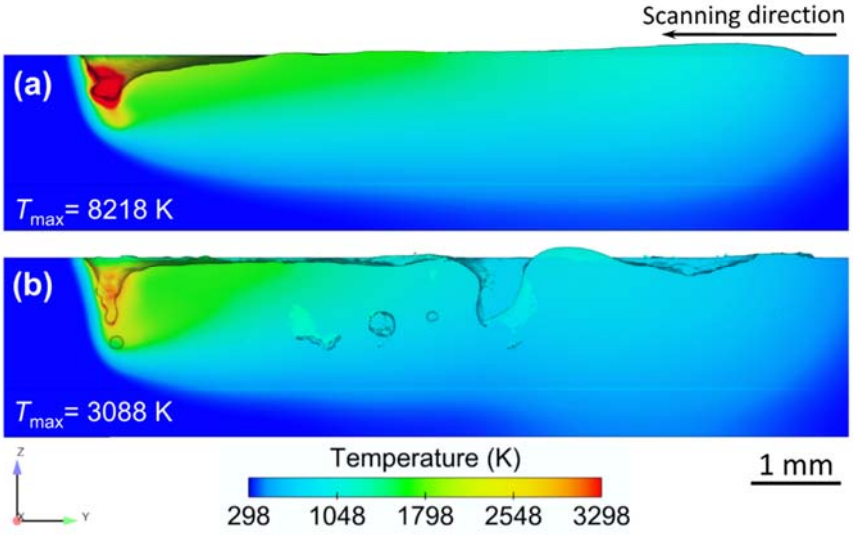


**Fig. 10.** CtFD simulated EBM melt beads processed with an $E_{\text{line}}$ of 12 J/mm and without preheating (room temperature, 298 K) under (a) vacuum and (b) standard atmospheric pressure.

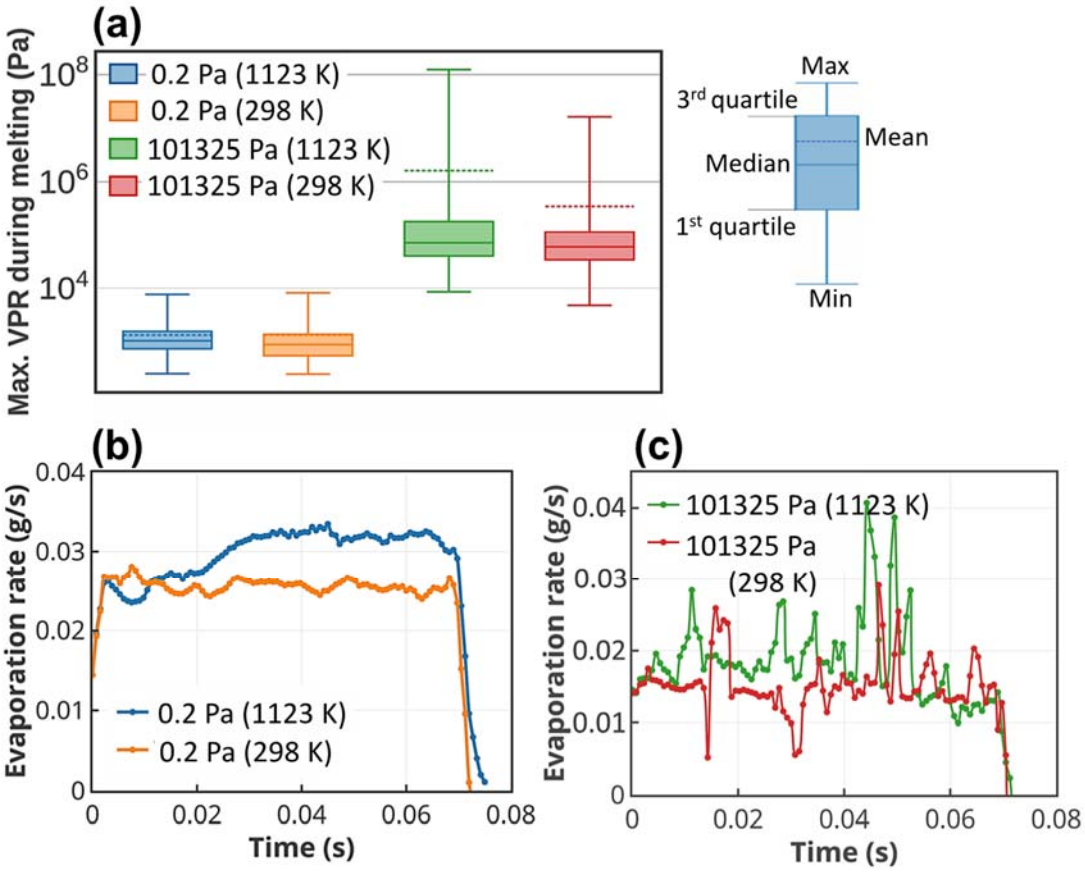


**Fig. 11.** (a) Combined simulation results of the maximum vapor recoil pressure in EBM under an $E_{\text{line}}$ of 12 J/mm and using the two initial temperatures. The enhancements of vapor recoil pressures under (b) vacuum and (c) standard atmospheric pressure were due to the increase in the metal evaporation rate with an increase in the initial temperature.

### *4.3 Influence of absorption and interaction of energy beam with materials*

The characteristics of the heat source determine the energy absorption. In EBM, when fast-moving electrons strike a metal, the electrons penetrate the molecular lattice of the material, and the kinetic energy of the electrons is almost entirely absorbed to heat the material instantly. Comparatively, in SLM, the laser photons are focused on the metal surface to melt the material by radiant heat. The ways of absorbing heat are very different between EBM and SLM. A major issue in SLM is that laser reflection from mirror-like molten metals can reflect some of the laser photons. In particular, when a laser irradiates a melt depression, the laser can be repeatedly reflected and absorbed between the interior surfaces of the melt depression [24][25]. Such multiple laser reflections improve the heat absorption from the laser. To study the influence of the multiple laser

reflections on the molten pool behavior, a simulation without multiple reflections was implemented by invalidating the second reflection. Fig. 12 shows the CtFD-simulated SLM melt beads with and without multiple reflections using the same *P* and *V*. It can be observed that, without multiple reflections, the keyhole-induced porosity was significantly lower. Fig. 13 shows the CtFD simulated SLM melting processes with and without multiple reflections of the laser over time; the red arrow indicates the reflected laser tracing. The depression depth of the molten pool front decreased with decreasing laser reflection. Shallow melt depression helped to improve the molten pool stability and further avoid keyhole formation. As shown in Fig. 14, the shallow melt depression was caused by the decrease in the heat flux absorbed from the laser when multiple reflections were invalidated. This analysis reveals that under high-energy conditions, the molten pool instability of SLM under atmospheric pressure mainly resulted from the recoil pressure caused by evaporation. When the melt depression was formed, the multiple laser reflections inside the depression increased the heat absorption rate, thereby increasing the evaporation amount and making the melt depression deeper and sharper. Eventually, keyhole collapse easily occurred and formed pores.

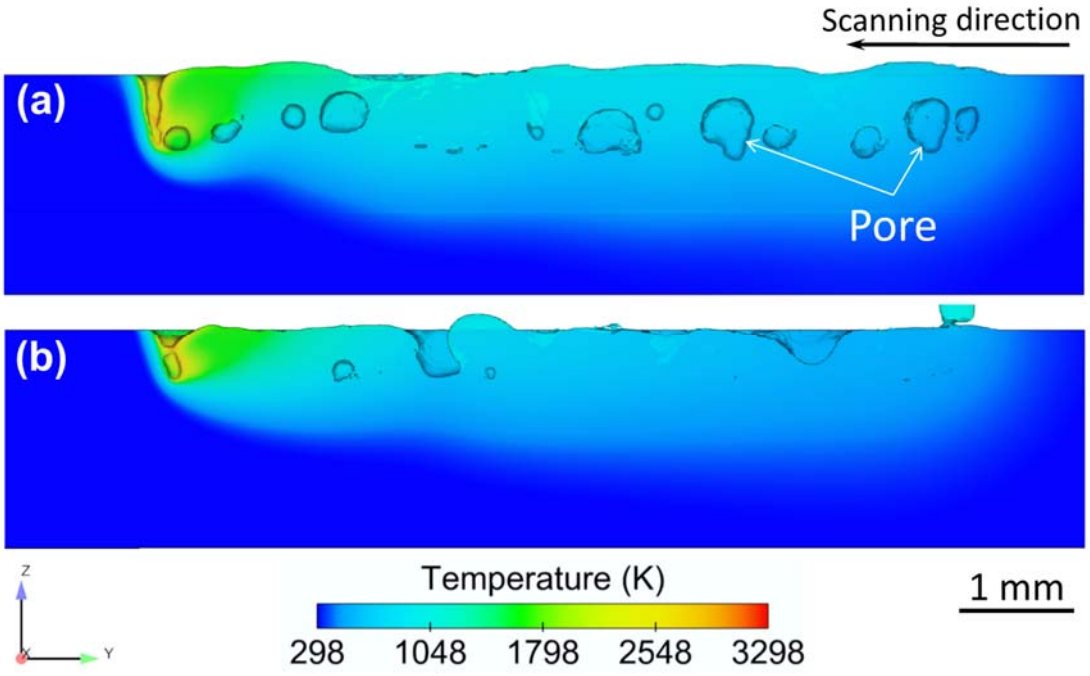


**Fig. 12.** CtFD simulated SLM melt beads processed with an $E_{\text{line}}$ of 12 J/mm (a) with and (b) without multiple laser reflections.

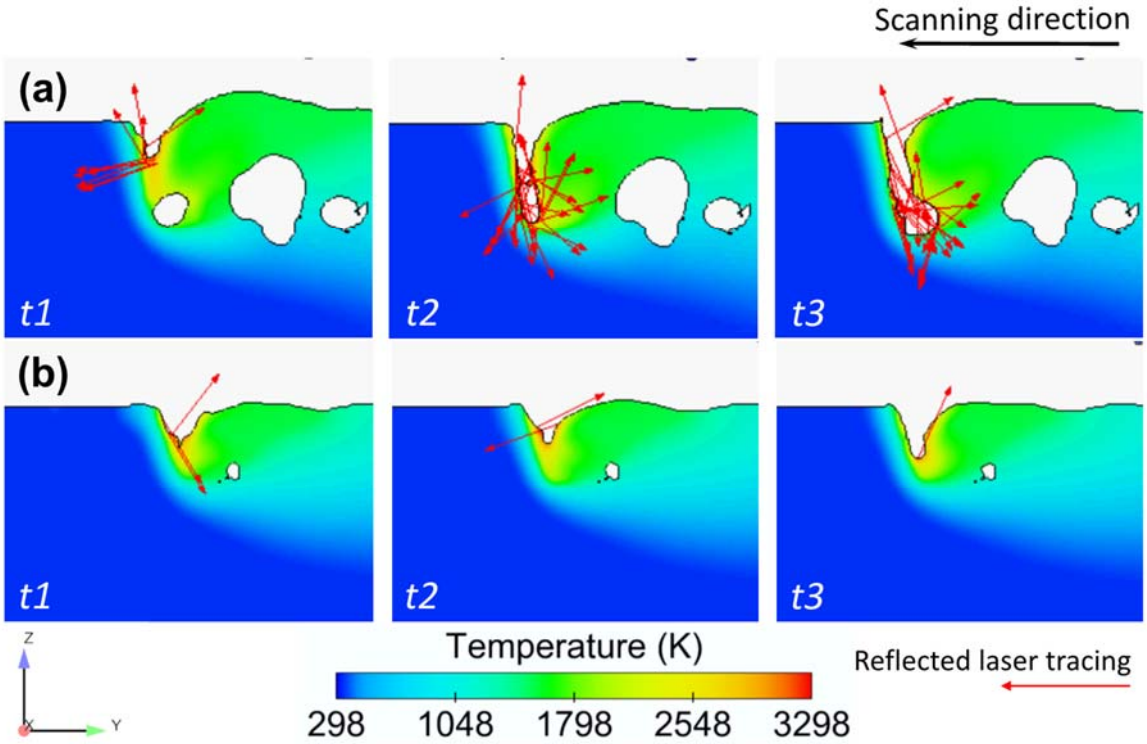


**Fig. 13.** CtFD simulated SLM melting processes (a) with and (b) without multiple laser reflections over time under an $E_{\text{line}}$ of 12 J/mm. Reflected laser tracing is denoted by a red arrow.

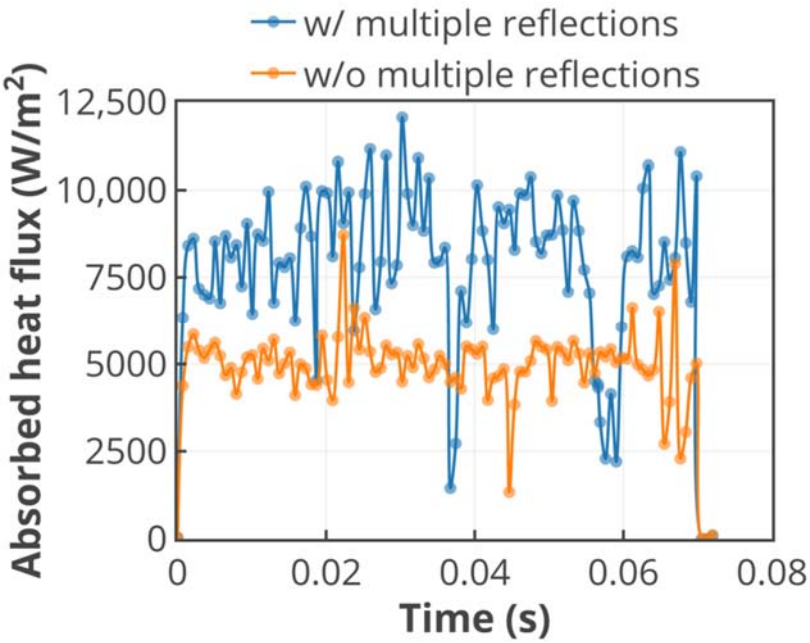


**Fig. 14.** Simulation results of heat flux absorbed from the laser in SLM melting processes with and without multiple laser reflections over time under an $E_{\text{line}}$ of 12 J/mm.

### *4.4 Summary and prospect*

The above results confirm the possibility of improving the molten pool instability and suppress defects by manipulating the operating and environmental conditions in EBM and SLM. Although the above results were derived by using a CCM alloy, they are applicable to other metal materials. Notably, as metal parts are built by powder bed fusion in a track-by-track and layer-by-layer manner, the remelting process between tracks and layers is important for defect suppression. Applying preheating can increase the melt width and depth, thereby suppressing the lack of fusion between tracks and layers and extending the lower limit of the energy input in the process window. The porosity originated in the previously solidified track or layer can be partially mitigated or fixed by a remelting process. However, the new porosity induced by the instable melt within the subsequently deposited track or layer is inevitable if the process parameters are unchanged. The forming quality of the as-built parts depends on the stable and flawless melt tracks. Reducing the keyhole-induced porosity in the melt track by lowering the ambient pressure can extend the higher limit of the energy input in the process window.

The present study focused on the comparison of the fundamental molten pool dynamics in EBM and SLM. Thus, this study is limited because no powder layer was considered in the experiments and simulations. Both the typical powder size with corresponding layer thickness and the energy transfer phenomenon depending on the particle size distribution are different between EBM and SLM. In a future study, we will investigate the influence of the powder layer on the dynamics of EBM and SLM molten pools.

## 5. Conclusions

Single-bead melting experiments were performed using EBM and SLM in conjunction with CtFD simulations under high-energy conditions to clarify the role of the operating and environmental conditions in the determination of the molten pool dynamics. The main conclusions are summarized as follows:

1) Owing to the slight vapor recoil pressure under vacuum, EBM tended to maintain melting in the conduction mode, whereas SLM was more likely to melt in keyhole mode under high-energy conditions.

2) Experimental X-CT results and numerical simulation showed that as the energy input increased, the keyhole-induced pores were more likely to appear in the melt bead processed by SLM.
3) The instantaneous maximum temperature of the SLM molten pool was much lower than that of the EBM molten pool, which was due to the intense heat convection during SLM under standard atmospheric pressure. Compared to EBM, the higher ambient pressure in SLM increased the effect of the vapor recoil pressure on the melt surface.
4) Increasing the initial temperature strengthened the vapor recoil pressure owing to the increase in the metal evaporation rate. However, the vapor recoil pressures under vacuum remained considerably low in EBM with preheating.
5) In SLM, the multiple laser reflections inside the melt depression increased the heat absorption rate, thereby increasing the evaporation and making the melt depression deeper and sharper. This caused keyhole collapse and pore formation.

**Acknowledgments**

This work was supported by the Japan Ministry of Economy, Trade and Industry (METI), the New Energy and Industrial Technology Development Organization (NEDO), the Technology Research Association for Future Additive Manufacturing (TRAFAM), and JSPS KAKENHI Grant Number JP18054020 and JP18041448. We would like to thank Editage (www.editage.com) for English language editing.

**Appendix**

*A1. Fluid convection in CtFD modeling*

Buoyant convection occurs as the fluid density varies owing to thermal expansion. By introducing a temperature-dependent density, the buoyancy effect is activated. The density of a solid CCM alloy can be calculated from thermal expansion data [66]. The temperature-dependent density of the liquid alloy was estimated using an empirical equation derived by Valencia [67]. In addition, the Marangoni effect is a result of the temperature-dependent surface tension:

$$\gamma(T) = \gamma_{\mathrm{L}} + \frac{d\gamma}{dT}(T - T_{\mathrm{L}}), \tag{A.1}$$

where $\gamma_L$ is the referenced surface tension (J/m$^2$) at the liquidus, and $d\gamma/dT$ denotes the temperature coefficient of surface tension (J/m$^2$·K). Therefore, the Marangoni force, which acts along the surface tangent and drives the Marangoni convection, is expressed as

$$\frac{d\gamma}{dx} = \frac{d\gamma}{dT}\nabla T, \tag{A.2}$$

where $\nabla T$ is the temperature gradient (K/m) along the fluid surface.

*A2. Heat transfer in CtFD modeling*

In addition to the thermal conduction $j^*$, we introduce the heat radiation, which is expressed by the Stefan–Boltzmann law:

$$j^* = \varepsilon\sigma(T^4 - T_0^4), \tag{A.3}$$

where $\varepsilon$ is the material emissivity, $\sigma$ is the Stefan–Boltzmann constant (W/m$^2$·K$^4$), and $T_0$ is the ambient temperature (K). Moreover, the heat loss due to evaporative cooling when the temperature of the liquid surface $T$ exceeds the saturation temperature $T_V$ is described as [68]

$$q_{vap} = \frac{0.82\Delta H^*}{\sqrt{2\pi MRT}} p_0 \exp\left[\frac{\Delta H^*(T - T_V)}{RTT_V}\right], \tag{A.4}$$

where $M$ is the vapor molar mass, and $\Delta H^*$ is the effective enthalpy (J/kg), which is expressed as

$$\Delta H^* = \Delta H_{LV} + \frac{k(k+1)RT}{2(k-1)}. \tag{A.5}$$

*A3. Physical properties of CCM alloy and coefficients/constants applied in CtFD simulation*

The parameters applied in the numerical simulation are listed in Table A.1.

**Table A.1.** Physical properties of CCM alloy and coefficients/constants applied in the simulation

| Name | Symbol and unit | Value |
|---|---|---|
| Density | $\rho$ (g/cm$^3$) | 8.28~7.13 |
| Viscosity | $\mu$ (mPa · s) | 5.6~7.9 |
| Thermal conductivity | $\kappa$ (W/m · K) | 14.5~37.6 |

| | | |
|---|---|---|
| Specific heat | $C_{\mathrm{P}}$ (J/kg · K) | 465~760 |
| Emissivity | $\varepsilon$ | 0.23 |
| Liquidus temperature | $T_{\mathrm{L}}$ (K) | 1703 |
| Solidus Temperature | $T_{\mathrm{S}}$ (K) | 1623 |
| Boiling point at standard atmospheric pressure | $T_{\mathrm{V1}}$ (K) | 3225 |
| Latent heat of fusion | $\Delta H_{\mathrm{SL}}$ (J/kg) | 3.14e+05 |
| Latent heat of vaporization | $\Delta H_{\mathrm{LV}}$ (J/kg) | 6.34e+06 |
| Surface tension at $T_{\mathrm{L}}$ | $\gamma_{\mathrm{L}}$ (J/m$^2$) | 1.85 |
| Temperature coefficient of surface tension | $\frac{d\gamma}{dT}$(J/m$^2$ · K) | -0. 00043 |
| Adiabatic index | $k$ | 1.66 |
| Stefan-Boltzmann constant | $\sigma$ (W/m$^2$ · K$^4$) | 5.67e-08 |
| Universal gas constant | $R$ (J/K · mol) | 8.314 |
| Environment temperature | $T_0$ (K) | 298 |

*A4. Parameters of X-CT measurement*

The parameters of the X-CT measurement are listed in Table A.2.

**Table A.2.** Measurement conditions and related parameters of X-CT measurements

| Name | Value |
|---|---|
| X-ray voltage | 150 kV |
| X-ray current | 66 μA |
| Inclined angle | 0° |
| Pixel size | 0.0495 mm |
| Nominal resolution | 7 μm |
| Addition count (mean) | 6 |
| Addition count (sum) | 1 |
| Addition rate | 1 (frame/second) |
| Save projection | 400 |

| | |
|---|---|
| Imaging matrix (width) | 2304 |
| Imaging matrix (height) | 1300 |
| Scan time | 39.9 (min) |

**References**


[1] C. Körner, Additive manufacturing of metallic components by selective electron beam melting — a review, International Materials Reviews. 61 (2016) 361–377. doi:10.1080/09506608.2016.1176289.

[2] M. Galati, L. Iuliano, A literature review of powder-based electron beam melting focusing on numerical simulations, Additive Manufacturing. 19 (2018) 1–20. doi:10.1016/j.addma.2017.11.001.

[3] P.K. Gokuldoss, S. Kolla, J. Eckert, Additive manufacturing processes: Selective laser melting, electron beam melting and binder jetting-selection guidelines, Materials. 10 (2017) 672. doi:10.3390/ma10060672.

[4] M. Galati, L. Iuliano, A. Salmi, E. Atzeni, Modelling energy source and powder properties for the development of a thermal FE model of the EBM additive manufacturing process, Additive Manufacturing. 14 (2017) 49–59. doi:10.1016/j.addma.2017.01.001.

[5] M.S. Brown, C.B. Arnold, Fundamentals of Laser-Material Interaction and Application to Multiscale Surface Modification, in: Springer Series in Materials Science, Springer Verlag, 2010: pp. 91–120. doi:10.1007/978-3-642-10523-4_4.

[6] C. Körner, A. Bauereiß, E. Attar, Fundamental consolidation mechanisms during selective beam melting of powders, Modelling and Simulation in Materials Science and Engineering. 21 (2013) 085011. doi:10.1088/0965-0393/21/8/085011.

[7] H. Gong, K. Rafi, H. Gu, G.D. Janaki Ram, T. Starr, B. Stucker, Influence of defects on mechanical properties of Ti-6Al-4V components produced by selective laser melting and electron beam melting, Materials and Design. 86 (2015) 545–554. doi:10.1016/j.matdes.2015.07.147.

[8] Y.J. Liu, S.J. Li, H.L. Wang, W.T. Hou, Y.L. Hao, R. Yang, T.B. Sercombe, L.C. Zhang, Microstructure, defects and mechanical behavior of beta-type titanium porous structures

manufactured by electron beam melting and selective laser melting, Acta Materialia. 113 (2016) 56–67. doi:10.1016/j.actamat.2016.04.029.

[9] D. Greitemeier, F. Palm, F. Syassen, T. Melz, Fatigue performance of additive manufactured TiAl6V4 using electron and laser beam melting, International Journal of Fatigue. 94 (2017) 211–217. doi:10.1016/j.ijfatigue.2016.05.001.

[10] H. Wang, B. Zhao, C. Liu, C. Wang, X. Tan, M. Hu, A Comparison of Biocompatibility of a Titanium Alloy Fabricated by Electron Beam Melting and Selective Laser Melting, PLOS ONE. 11 (2016) e0158513. doi:10.1371/journal.pone.0158513.

[11] B. Zhao, H. Wang, N. Qiao, C. Wang, M. Hu, Corrosion resistance characteristics of a Ti-6Al-4V alloy scaffold that is fabricated by electron beam melting and selective laser melting for implantation in vivo, Materials Science and Engineering C. 70 (2017) 832–841. doi:10.1016/j.msec.2016.07.045.

[12] H. Gong, K. Rafi, H. Gu, T. Starr, B. Stucker, Analysis of defect generation in Ti-6Al-4V parts made using powder bed fusion additive manufacturing processes, Additive Manufacturing. 1 (2014) 87–98. doi:10.1016/j.addma.2014.08.002.

[13] C. Qiu, C. Panwisawas, M. Ward, H.C. Basoalto, J.W. Brooks, M.M. Attallah, On the role of melt flow into the surface structure and porosity development during selective laser melting, Acta Materialia. 96 (2015) 72–79. doi:10.1016/j.actamat.2015.06.004.

[14] D. Gu, M. Xia, D. Dai, On the role of powder flow behavior in fluid thermodynamics and laser processability of Ni-based composites by selective laser melting, International Journal of Machine Tools and Manufacture. 137 (2019) 67–78. doi:10.1016/j.ijmachtools.2018.10.006.

[15] Y. Zhao, Y. Koizumi, K. Aoyagi, K. Yamanaka, A. Chiba, Manipulating local heat accumulation towards controlled quality and microstructure of a Co-Cr-Mo alloy in powder bed fusion with electron beam, Materials Letters. 254 (2019) 269–272. doi:10.1016/j.matlet.2019.07.078.

[16] Y.S. Lee, M.M. Kirka, J. Ferguson, V.C. Paquit, Correlations of cracking with scan strategy and build geometry in electron beam powder bed additive manufacturing, Additive Manufacturing. 32 (2020) 101031. doi:10.1016/j.addma.2019.101031.

[17] L. Scime, J. Beuth, Melt pool geometry and morphology variability for the Inconel 718 alloy in a laser powder bed fusion additive manufacturing process, Additive Manufacturing. 29 (2019) 100830. doi:10.1016/j.addma.2019.100830.

[18] C.L.A. Leung, S. Marussi, R.C. Atwood, M. Towrie, P.J. Withers, P.D. Lee, In situ X-ray imaging of defect and molten pool dynamics in laser additive manufacturing, Nature Communications. 9 (2018) 1–9. doi:10.1038/s41467-018-03734-7.

[19] H. Wong, D. Neary, E. Jones, P. Fox, C. Sutcliffe, Pilot feedback electronic imaging at elevated temperatures and its potential for in-process electron beam melting monitoring, Additive Manufacturing. 27 (2019) 185–198. doi:10.1016/j.addma.2019.02.022.

[20] C.L.A. Leung, S. Marussi, M. Towrie, J. del Val Garcia, R.C. Atwood, A.J. Bodey, J.R. Jones, P.J. Withers, P.D. Lee, Laser-matter interactions in additive manufacturing of stainless steel SS316L and 13-93 bioactive glass revealed by in situ X-ray imaging, Additive Manufacturing. 24 (2018) 647–657. doi:10.1016/j.addma.2018.08.025.

[21] Z. Gan, G. Yu, X. He, S. Li, Surface-active element transport and its effect on liquid metal flow in laser-assisted additive manufacturing, International Communications in Heat and Mass Transfer. 86 (2017) 206–214. doi:10.1016/j.icheatmasstransfer.2017.06.007.

[22] H. Salem, L.N. Carter, M.M. Attallah, H.G. Salem, Influence of processing parameters on internal porosity and types of defects formed in Ti6Al4V lattice structure fabricated by selective laser melting, Materials Science and Engineering A. 767 (2019) 138387. doi:10.1016/j.msea.2019.138387.

[23] Y. Yang, D. Gu, D. Dai, C. Ma, Laser energy absorption behavior of powder particles using ray tracing method during selective laser melting additive manufacturing of aluminum alloy, Materials and Design. 143 (2018) 12–19. doi:10.1016/j.matdes.2018.01.043.

[24] M. Bayat, A. Thanki, S. Mohanty, A. Witvrouw, S. Yang, J. Thorborg, N.S. Tiedje, J.H. Hattel, Keyhole-induced porosities in Laser-based Powder Bed Fusion (L-PBF) of Ti6Al4V: High-fidelity modelling and experimental validation, Additive Manufacturing. 30 (2019) 100835. doi:10.1016/j.addma.2019.100835.

[25] A. Bauereiß, T. Scharowsky, C. Körner, Defect generation and propagation mechanism during additive manufacturing by selective beam melting, Journal of Materials Processing Technology. 214 (2014) 2522–2528. doi:10.1016/J.JMATPROTEC.2014.05.002.

[26] A. Klassen, V.E. Forster, V. Juechter, C. Körner, Numerical simulation of multi-component evaporation during selective electron beam melting of TiAl, Journal of Materials Processing Technology. 247 (2017) 280–288. doi:10.1016/J.JMATPROTEC.2017.04.016.

[27] W. Yan, W. Ge, J. Smith, S. Lin, O.L. Kafka, F. Lin, W.K. Liu, Multi-scale modeling of electron beam melting of functionally graded materials, Acta Materialia. 115 (2016) 403–412. doi:10.1016/j.actamat.2016.06.022.

[28] W. Yan, Y. Qian, W. Ge, S. Lin, W.K. Liu, F. Lin, G.J. Wagner, Meso-scale modeling of multiple-layer fabrication process in Selective Electron Beam Melting: Inter-layer/track voids formation, Materials & Design. 141 (2018) 210–219. doi:10.1016/J.MATDES.2017.12.031.

[29] S.A. Khairallah, A.T. Anderson, A. Rubenchik, W.E. King, Laser powder-bed fusion additive manufacturing: Physics of complex melt flow and formation mechanisms of pores, spatter, and denudation zones, Acta Materialia. 108 (2016) 36–45. doi:10.1016/j.actamat.2016.02.014.

[30] M.J. Matthews, G. Guss, S.A. Khairallah, A.M. Rubenchik, P.J. Depond, W.E. King, Denudation of metal powder layers in laser powder bed fusion processes, Acta Materialia. 114 (2016) 33–42. doi:10.1016/j.actamat.2016.05.017.

[31] J.J.S. Dilip, S. Zhang, C. Teng, K. Zeng, C. Robinson, D. Pal, B. Stucker, Influence of processing parameters on the evolution of melt pool, porosity, and microstructures in Ti-6Al-4V alloy parts fabricated by selective laser melting, Progress in Additive Manufacturing. 2 (2017) 157–167. doi:10.1007/s40964-017-0030-2.

[32] J. Gockel, J. Beuth, K. Taminger, Integrated control of solidification microstructure and melt pool dimensions in electron beam wire feed additive manufacturing of ti-6al-4v, Additive Manufacturing. 1 (2014) 119–126. doi:10.1016/j.addma.2014.09.004.

[33] X. Ding, Y. Koizumi, D. Wei, A. Chiba, Effect of process parameters on melt pool geometry and microstructure development for electron beam melting of IN718: A systematic single bead analysis study, Additive Manufacturing. 26 (2019) 215–226. doi:10.1016/j.addma.2018.12.018.

[34] M. Galati, A. Snis, L. Iuliano, Experimental validation of a numerical thermal model of the EBM process for Ti6Al4V, Computers and Mathematics with Applications. 78 (2019) 2417–2427. doi:10.1016/j.camwa.2018.07.020.

[35] GE, Arcam EBM A2X - EBM Machine| GE Additive, (n.d.). https://www.ge.com/additive/additive-manufacturing/machines/ebm-machines/arcam-ebm-a2x (accessed June 2, 2020).

[36] ConceptLaser, Concept Laser M2 cusing, (n.d.). http://www.4c.com.tr/en/m2-cusing.html (accessed June 2, 2020).

[37] M. Galati, P. Minetola, G. Rizza, Surface roughness characterisation and analysis of the Electron Beam Melting (EBM) process, Materials. 12 (2019). doi:10.3390/ma12132211.

[38] *FLOW-3D*® Version 11.2 [Computer software]. (2017). Santa Fe, NM: Flow Science, Inc. https://www.flow3d.com.

[39] Y.S. Lee, W. Zhang, Modeling of heat transfer, fluid flow and solidification microstructure of nickel-base superalloy fabricated by laser powder bed fusion, Additive Manufacturing. 12 (2016) 178–188. doi:10.1016/j.addma.2016.05.003.

[40] H. Wang, Y. Zou, Microscale interaction between laser and metal powder in powder-bed additive manufacturing: Conduction mode versus keyhole mode, International Journal of Heat and Mass Transfer. 142 (2019). doi:10.1016/j.ijheatmasstransfer.2019.118473.

[41] S.A. Khairallah, A. Anderson, A.M. Rubenchik, J. Florando, S. Wu, H. Lowdermilk, Simulation of the main physical processes in remote laser penetration with large laser spot size, AIP Advances. 5 (2015) 047120. doi:10.1063/1.4918284.

[42] J. Schou, Risø, Laser-beam interactions with materials: Physical principles and applications, Nuclear Instruments and Methods in Physics Research Section B: Beam Interactions with Materials and Atoms. 124 (1997) 647–648. doi:10.1016/S0168-583X(97)00111-0.

[43] N. Shen, K. Chou, Thermal modeling of electron beam additive manufacturing process - Powder sintering effects, in: ASME 2012 International Manufacturing Science and Engineering Conference Collocated with the 40th North American Manufacturing Research Conference and in Participation with the Int. Conf., MSEC 2012, 2012: pp. 287–295. doi:10.1115/MSEC2012-7253.

[44] J.H. Cho, S.J. Na, Implementation of real-time multiple reflection and Fresnel absorption of laser beam in keyhole, Journal of Physics D: Applied Physics. 39 (2006) 5372–5378. doi:10.1088/0022-3727/39/24/039.

[45] H.E. Cline, T.R. Anthony, Heat treating and melting material with a scanning laser or electron beam, Journal of Applied Physics. 48 (1977) 3895–3900. doi:10.1063/1.324261.

[46] P. Bidare, I. Bitharas, R.M. Ward, M.M. Attallah, A.J. Moore, Fluid and particle dynamics in laser powder bed fusion, Acta Materialia. 142 (2018) 107–120. doi:10.1016/j.actamat.2017.09.051.

[47] D. Wang, S. Wu, F. Fu, S. Mai, Y. Yang, Y. Liu, C. Song, Mechanisms and characteristics of spatter generation in SLM processing and its effect on the properties, Materials and Design. 117 (2017) 121–130. doi:10.1016/j.matdes.2016.12.060.

[48] S.A. Khairallah, A.A. Martin, J.R.I. Lee, G. Guss, N.P. Calta, J.A. Hammons, M.H. Nielsen, K. Chaput, E. Schwalbach, M.N. Shah, M.G. Chapman, T.M. Willey, A.M. Rubenchik, A.T. Anderson, Y.M. Wang, M.J. Matthews, W.E. King, Controlling interdependent meso-nanosecond dynamics and defect generation in metal 3D printing, Science. 368 (2020) 660–665. doi:10.1126/science.aay7830.

[49] X. Chen, H. Tian, Z. Yan, X. Zhi, J. Zhang, Z. Yuan, Investigation on mechanism of surface tension on morphology of melt track in selective laser melting processing, Applied Physics A: Materials Science and Processing. 124 (2018) 1–7. doi:10.1007/s00339-018-2102-7.

[50] M.F. Zäh, S. Lutzmann, Modelling and simulation of electron beam melting, Production Engineering. 4 (2010) 15–23. doi:10.1007/s11740-009-0197-6.

[51] C.D. Boley, S.A. Khairallah, A.M. Rubenchik, Calculation of laser absorption by metal powders in additive manufacturing, Applied Optics. 54 (2015) 2477. doi:10.1364/ao.54.002477.

[52] C.L.A. Leung, R. Tosi, E. Muzangaza, S. Nonni, P.J. Withers, P.D. Lee, Effect of preheating on the thermal, microstructural and mechanical properties of selective electron beam melted Ti-6Al-4V components, Materials and Design. 174 (2019). doi:10.1016/j.matdes.2019.107792.

[53] A.M. Kiss, A.Y. Fong, N.P. Calta, V. Thampy, A.A. Martin, P.J. Depond, J. Wang, M.J. Matthews, R.T. Ott, C.J. Tassone, K.H. Stone, M.J. Kramer, A. van Buuren, M.F. Toney, J. Nelson Weker, Laser-Induced Keyhole Defect Dynamics during Metal Additive Manufacturing, Advanced Engineering Materials. 21 (2019) 1900455. doi:10.1002/adem.201900455.

[54] H. Bian, K. Aoyagi, Y. Zhao, C. Maeda, T. Mouri, A. Chiba, Microstructure refinement for superior ductility of Al–Si alloy by electron beam melting, Additive Manufacturing. 32 (2020) 100982. doi:10.1016/j.addma.2019.100982.

[55] K.Q. Le, C. Tang, C.H. Wong, On the study of keyhole-mode melting in selective laser melting process, International Journal of Thermal Sciences. 145 (2019) 105992. doi:10.1016/j.ijthermalsci.2019.105992.

[56] Y. Zhao, Y. Koizumi, K. Aoyagi, D. Wei, K. Yamanaka, A. Chiba, Molten pool behavior and effect of fluid flow on solidification conditions in selective electron beam melting (SEBM) of a biomedical Co-Cr-Mo alloy, Additive Manufacturing. 26 (2019) 202–214. doi:10.1016/j.addma.2018.12.002.

[57] A. Raghavan, H.L. Wei, T.A. Palmer, T. DebRoy, Heat transfer and fluid flow in additive manufacturing, Journal of Laser Applications. 25 (2013) 052006. doi:10.2351/1.4817788.

[58] P. Bidare, I. Bitharas, R.M. Ward, M.M. Attallah, A.J. Moore, Laser powder bed fusion at sub-atmospheric pressures, International Journal of Machine Tools and Manufacture. 130–131 (2018) 65–72. doi:10.1016/j.ijmachtools.2018.03.007.

[59] N.P. Calta, A.A. Martin, J.A. Hammons, M.H. Nielsen, T.T. Roehling, K. Fezzaa, M.J. Matthews, J.R. Jeffries, T.M. Willey, J.R.I. Lee, Pressure dependence of the laser-metal interaction under laser powder bed fusion conditions probed by in situ X-ray imaging, Additive Manufacturing. 32 (2020). doi:10.1016/j.addma.2020.101084.

[60] B. Zhou, J. Zhou, H. Li, F. Lin, A study of the microstructures and mechanical properties of Ti6Al4V fabricated by SLM under vacuum, Materials Science and Engineering A. 724 (2018) 1–10. doi:10.1016/j.msea.2018.03.021.

[61] A. V. Gusarov, T. Laoui, L. Froyen, V.I. Titov, Contact thermal conductivity of a powder bed in selective laser sintering, International Journal of Heat and Mass Transfer. 46 (2003) 1103–1109. doi:10.1016/S0017-9310(02)00370-8.

[62] R. Mertens, S. Dadbakhsh, J. Van Humbeeck, J.P. Kruth, Application of base plate preheating during selective laser melting, in: Procedia CIRP, Elsevier B.V., 2018: pp. 5–11. doi:10.1016/j.procir.2018.08.002.

[63] A. Iveković, M.L. Montero-Sistiaga, K. Vanmeensel, J.P. Kruth, J. Vleugels, Effect of processing parameters on microstructure and properties of tungsten heavy alloys fabricated by

SLM, International Journal of Refractory Metals and Hard Materials. 82 (2019) 23–30. doi:10.1016/j.ijrmhm.2019.03.020.

[64] I. Yadroitsev, P. Krakhmalev, I. Yadroitsava, S. Johansson, I. Smurov, Energy input effect on morphology and microstructure of selective laser melting single track from metallic powder, Journal of Materials Processing Technology. 213 (2013) 606–613. doi:10.1016/j.jmatprotec.2012.11.014.

[65] M. Malỳ, C. Höller, M. Skalon, B. Meier, D. Koutnỳ, R. Pichler, C. Sommitsch, D. Paloušek, Effect of process parameters and high-temperature preheating on residual stress and relative density of Ti6Al4V processed by selective laser melting, Materials. 16 (2019). doi:10.3390/ma12060930.

[66] CarTech, CarTech® BioDur® CCM® Alloy, (n.d.). http://cartech.ides.com/datasheet.aspx?i=101&E=8 (accessed June 2, 2020).

[67] J.J. Valencia, Thermophysical Properties Sources and Availability of Reliable Data, (2008). doi:10.1361/asmhba0005240.

[68] J.H. Cho, D.F. Farson, J.O. Milewski, K.J. Hollis, Weld pool flows during initial stages of keyhole formation in laser welding, Journal of Physics D: Applied Physics. 42 (2009) 175502. doi:10.1088/0022-3727/42/17/175502.